

# Basal force fluctuations and granular rheology: Linking macroscopic descriptions of granular flows to bed forces with implications for monitoring signals

P. Zrelak<sup>1</sup>, E. C. P. Breard<sup>1,2\*</sup>, J. Dufek<sup>1</sup>

<sup>1</sup>Department of Earth Sciences, University of Oregon, Eugene, Oregon, U.S.A

<sup>2</sup>School of Geosciences, The University of Edinburgh, Edinburgh, Scotland, U.K

## Key Points:

- Discrete element methods used to simulate granular flows in plane-shear and inclined-plane flow configurations recording contact forces
- Basal forces record changes in flow regime tracked by non-dimensional shear rate (inertial number) independent of flow configuration
- Basal forces can track flow rheology through bed-averaged inertial number, particle concentration, and granular temperature

---

\*Current address

Corresponding author: P.J. Zrelak, [pzrelak@uoregon.edu](mailto:pzrelak@uoregon.edu)

## Abstract

Granular flows are ubiquitous in nature with single flows traversing a wide range of dynamic conditions from initiation to deposition. Basal forces exerted by environmental granular flows are responsible for the generation of observable seismic signals. To fully realize the benefit of seismic measurements, basal granular forces must be linked to macroscopic internal flow dynamics across a wide range of flow conditions. We utilize discrete element simulations to observe dry and submerged granular flows under plane-shear and inclined flow configurations, relating bulk kinematics and rheology to basal forcing signals. We find that regardless of the flow geometry/initiation the variance in basal forcing scales with a local non-dimensional shear-rate (or inertial number  $I$ ), and this scaling tracks four different flow regimes spanned by our simulations: (1) an unsteady particle rearrangement regime when  $I < 10^{-3}$ , where basal forces are dominated by low frequencies; (2) an intermediate regime when  $10^{-3} < I < 10^{-2}$ , where granular temperature is isotropic and basal forces start to become noise-like, (3) a transitional regime at  $10^{-2} < I < 10^{-1}$ , where the increase in basal tractions with increasing shear-rates stalls as the granular bed dilates, partially destroying the contact network and configurational memory, and (4) a fully collisional regime when  $I > 10^{-1}$ , where granular temperature is anisotropic in the stream-wise direction, and the signal becomes white noise-like up to a cutoff frequency that is dependent on particle size and shear-rate. This effort suggests that basal forces, recorded in instrumented channels or inverted from seismic signals, can be used to interpret complex granular processes in geophysical flows.

## Plain Language Summary

Debris flows, pyroclastic flows, and debris avalanches are natural granular flows that have the ability to generate seismic signals. These signals can be recorded from safe distances away, providing a record of how these flows interact with the surface. Nevertheless, it is difficult to interpret these signals in terms of flow conditions. To better understand how to relate the forces exerted by these flows back to flow conditions, we perform simulations of granular flows, recording the forces exerted on a simulated substrate. Simulated flow conditions resemble those that correspond to beginning of an event, when the flow is slow moving, to conditions that are like that of a fast moving well developed flow. We find that the forces exerted on the ground have the ability to tell researchers important flow information, such as how stresses are transmitted internally in the flow. Moreover, these basal forces record when the collection of grains changes from a liquid-like to a gas-like flow, where individual grains are no longer in prolonged contact, but begin to collide and bounce off one another, like gas-molecules. These results show that complex information can be encoded in the interactions between an overriding flow and its substrate.

## 1 Introduction

Flowing granular mixtures are prevalent in nature. These so-called geophysical mass flows experience a variety of granular interactions due to spatio-temporal variations in particle concentration, particle-fluid-particle interactions, grain size distributions, and shear-rates. Phenomenon such as debris flows, pyroclastic density currents, and debris avalanches showcase complex phenomenological behavior that is intrinsic to granular materials. For example, debris flows are mixtures of water and particles that can span from dilute, near hyperconcentrated flow, conditions, to dense flows able to support large clasts (Iverson, 1997). Pyroclastic density currents, gravity flows of volcanic particles and gas, display enhanced mobility that is attributed to the liquid-like nature of gas fluidized granular flows and the development of pore pressure (Lube et al., 2019; Breard et al., 2023). Debris avalanches are large slope failures that can support coherent domains of rocks 10s of meters in size with runout distances of 10s of kilometers. These large events can tran-

sition from granular dominated to viscous-like flow due to fine particle enrichment and lubrication (Roverato et al., 2015). Each of these disparate phenomena can span from dry conditions, where particle inertia allows for drag effects to be neglected, to fluid immersed conditions, where fluid drag and pore pressure gradients become important (Delannay et al., 2017; Lube et al., 2020).

Nearly all geophysical mass flows can generate a detectable seismic signal upon their interaction with their substrate (Allstadt et al., 2018). A recorded seismic signal e.g., ground velocity  $\dot{u}(t)$  measured at some distance from the flow, is a result of a convolution of three functions:

$$\dot{u}(t) = F(t) * g(t) * r(t) \quad (1)$$

with  $F(t)$  being the fluctuating forces exerted onto the substrate,  $g(t)$  being a transfer function — known as the green’s function — representing path effects that attenuate and disperse forcing energy, and  $r(t)$  being the instrument impulse response (Fig. 1)(Stein & Wysession, 2003). Much effort has been invested in utilizing geophysical signals to inform scientists and hazard coordinators, with the aim to improve detection and monitoring. For example, time and spectral characteristics of seismic signals have been used to train machine learning algorithms to detect debris flow events (Chmiel et al., 2021); seismic envelopes have been correlated to event volume (Levy et al., 2015) and potential energy loss (Farin et al., 2018); and the ratio of horizontal and vertical ground displacements have been used to posit turbulent flow conditions (Cole et al., 2009; Walsh et al., 2020). Nevertheless, the link between internal dynamics and the source function  $F(t)$  is a non-trivial one. Allstadt et al. (2020) report data from controlled, large scale ( $8 - 10 \text{ m}^3$ ), debris flow experiments and calculated empirical green’s functions, constraining the path effects term  $g(t)$ . This allows the authors to invert basal tractions from seismic signals recorded by near-channel receivers. These inverted forces compare well with in-channel force plate measurements. Nevertheless, the authors were limited in their ability to use these inverted signals to infer detailed flow information due to the poorly constrained relationship between macroscopic flow dynamics and boundary forcing.

Measuring boundary forces (both experimentally and in numerical simulations) is important to understand not only how seismic forces are generated, but how flows affect and are affected by their environment. McCoy et al. (2013) measure basal forces in natural debris flows, relating these basal forces to channel incision. These authors leverage the high rate of debris flow events per year at their study site (Chalk Cliffs, CO), instrumenting the channel with a variety of sensors, creating a natural laboratory. Nevertheless, collecting data from real-world flows is difficult, providing the need for controlled experiments. Large scale debris flow experiments have been conducted at a controlled test site in Blue River, Oregon, USA since 1994 (Iverson et al., 2010). Here a wealth of data is collected, included load plates measuring boundary tractions generated by an overriding flow. These experiments not only provided data for Allstadt et al. (2020) but also for the development of depth-averaged models (Iverson & George, 2014; George & Iverson, 2014), and, in general, led to a more refined understanding of the physics of debris flows (Iverson, 1997). Large scale experiments are needed to reliably recreate near-scale geophysical flows. Nevertheless, as experimental scale increases, so does uncertainty. For example, near-scale experiments utilizing natural particles (e.g., sand and gravel) may have unideal shape and size distribution, which may lead to unforeseen phenomenon. Further, steady states are difficult to maintain when conducting large experiments. These uncertainties, paired with the resources required for conducting such experiments, highlights the need for smaller, scaled experiments. Researchers have utilized scaled experiments in various configurations to observe the probability distribution of boundary forces and the dynamical nature of these forces as they approach the jamming transition (Longhi et al., 2002; Corwin et al., 2005; Gardel et al., 2009; Kheiripour Langroudi et al., 2010). Other authors have looked at forces generated during individual particle-impact events, deriving scaling laws relating the mass and speed of the particle to energy transferred to the boundaries (Farin et al., 2015). Recent work has performed monodisperse inclined

slope flow experiments, recording basal forces at high frequencies, comparing these data to modeled data from stochastic impact models (Arran et al., 2021). Importantly, these authors find that the normalized squared basal force fluctuation, in the intermediate and high frequency ranges associated with uncorrelated particle interactions, is related to the bulk scaled shear-rate.

In the limit where grain-inertia dominates flow behaviour (e.g., unsaturated debris avalanches, the snouts of particle concentrated pyroclastic flows, and the coarse front of debris flows), substrate forcing, like bulk flow dynamics, is expected to be controlled by particle-particle interaction (Forterre & Pouliquen, 2008). Previous efforts show that sheared granular media span three distinct regimes that are related to the shear-rate: (1) stick-slip unsteady motion, (2) continuous deformation of the granular bed, (3) high energy collisional flow. The nature of particle velocity fluctuations are controlled by these regimes (Cruz et al., 2005). Velocity fluctuations are what give rise to a quantity referred to as granular temperature (Lun et al., 1984). Much like the thermal temperature of a gas, this quantity measures fluctuations in kinetic energy of individual particles in a system, generating a variance in the particle velocity distribution. While often treated as isotropic, heterogeneities in granular flows may give rise to local anisotropy in granular temperature, i.e. velocity fluctuations in different directions may vary in magnitude. As opposed to molecular gasses, granular systems are by definition in a perpetual state of dis-equilibrium due to energy being dissipated through inelastic particle-particle and particle-domain interactions (Goldhirsch, 2008). Trulsson et al. (2012) show that the dissipation mechanism in dense granular suspensions is a function of a confining pressure scaled by the interstitial fluid’s viscosity:  $\sqrt{\rho_s P_s} d / \eta_f = I / \sqrt{I_v}$ , where  $I$  is the inertial number from Cruz et al. (2005) and  $I_v$  is the viscous number from Boyer et al. (2011) (Eqs. (20) and (21), respectively). As this parameter approaches 10, contact forces increase rapidly to a limit where dissipation is controlled solely by particle contacts, and the flow behaves as a pure granular flow. In other terms, the dissipation mechanism in fluid immersed flows is dictated by the competition between confining (or solids) pressure, and viscous effects. Further, scaling laws relating wall friction to slip velocity scaled by velocity fluctuations provides evidence that fluctuations are key to describing dense flows near wall boundaries (Artoni & Richard, 2015). This suggests that flow information may be extracted from force fluctuations, or through the measurement of energy dissipation, near the flow-boundary.

Here we perform a series of 3D numerical experiments utilizing the discrete element method (DEM) to examine granular contributions to wall force fluctuations. The goal of this study is to relate macroscopic descriptions of granular flows to basal forcing under ideal conditions but over a wide range of inertial numbers. We will first briefly describe our methods, pointing the reader to preceding studies that advanced these efforts. Then, in Section 3, we will detail bed-averaged flow conditions, afterwards discussing wall-flow interactions in Section 3.2. We will close with a discussion relating the two observations culminating in a phase space spanned by our data in Section 4.2.

## 2 Methods

### 2.1 MFiX-DEM

Our 3D numerical experiments are conducted using the Department of Energy MFiX-DEM solver. Detailed information on MFiX-DEM is discussed in (Garg et al., 2012). MFiX-DEM solves the ordinary differential equations governing the motion of the  $i^{th}$  particle belonging to the  $m^{th}$  solid phase

$$m_i \frac{d\mathbf{V}_i}{dt} = m_i \mathbf{g} + \mathbf{F}_{d(i \in k, m)}(t) + \mathbf{F}_c(t) \quad (2)$$

where  $\mathbf{V}_i$  is the velocity of the particle,  $\mathbf{g}$  is the gravity vector,  $F_c(t)$  is the net contact forces associated with contacting particles,  $m_i$  is the mass of the  $i^{th}$  particle, and  $F_{d(i \in k, m)}(t)$



is the drag forces acting on the  $i^{th}$  particle, belonging to the  $m^{th}$  solid phase and  $k^{th}$  computational cell. Here, the added mass and history terms of the generalized Basset-Boussinesq-Oseen equation, arising due to unsteady fluid flow relative to the solid particles, are neglected (Maxey & Riley, 1983). We use the soft-sphere approach to particle contacts, modeling collisions and particle overlap as interactions between systems composed of springs and dashpots. In this way, the spring supplies the energy for rebound, gaining potential energy during collision and releasing post-collision; the dashpot simulates dissipation due to inelasticity. Thus, the net contact force in (2), in the normal direction, becomes a sum of the elastic and viscous components

$$F_c^n = F_k^n + F_\eta^n = -(k_n \delta_n + \eta_n |V_n^i - V_n^j|) \quad (3)$$

where superscripts (as well as subscripts in subsequent equations)  $n$  represent parameters in the normal direction. The elastic contribution in (3) is controlled by the elastic coefficient  $k_n$  and the particle overlap in the normal direction,  $\delta_n$ . The viscous contribution is a function of the dampening coefficient  $\eta_n$  and the relative normal velocities of the  $i^{th}$  and  $j^{th}$  contacting particles. The dampening coefficient is dictated by the elastic coefficient, normal coefficient of restitution  $e_n$ , and the effective mass between the two colliding particles

$$\eta_n = \frac{2\sqrt{m_{\text{eff}} k_n} |\ln e_n|}{\sqrt{\pi + \ln^2 e_n}} \quad (4)$$

Tangential elastic and viscous coefficients are related to their normal counterparts by a simple scale factor (i.e.  $k_t = \frac{2}{5}k_n$  and  $\eta_t = \frac{2}{7}\eta_n$ ). The minimum collision time between two particles is dictated by the elastic and viscous coefficients:

$$t_n^{\text{col}} = \pi \left( \frac{k_n}{m_{\text{eff}}} - \frac{-\eta_n^2}{4m_{\text{eff}}^2} \right)^{-1/2} \quad (5)$$

Timesteps are set to  $0.2t_n^{\text{col}}$  to resolve collisional interactions.

In the case where particles are submerged in a fluid, continuum mechanics are introduced and the fluid is governed by continuity and momentum conservation detailed in (Syamlal et al., 1993):

$$\frac{D}{Dt}(\epsilon_f \rho_f \mathbf{u}_f) = \nabla \cdot \bar{\bar{S}}_f + \epsilon_f \rho_f \mathbf{g} - \sum_{m=1}^M \mathbf{I}_{fm} \quad (6)$$

Where  $D/Dt$  is the material time derivative,  $\epsilon_f$  is the fluid volume fraction,  $\rho_f$  is the fluid density,  $\mathbf{u}_f$  is the fluid velocity, and  $\bar{\bar{S}}_f$  is the fluid phase stress tensor. Coupling between the continuous (fluid) and discrete (solid) phases is incorporated in the interphase momentum exchange term  $\mathbf{I}_{fm}$ , which is derived from the drag force in (2):

$$\mathbf{I}_{fm}^k = \frac{1}{\nu_k} \sum_{i=1}^{N_m} \mathbf{F}_d^{i \in k, m} K(\mathbf{X}_m^i, \mathbf{x}_k) \quad (7)$$

This states that the interphase momentum exchange is dictated by the particle drag force  $\mathbf{F}_d^{i \in k, m}$  associated with a particle residing within the  $k^{th}$  computation cell with a volume  $\nu_k$ . The particle force within the cell is modulated by the kernel  $K(\mathbf{X}_m^i, \mathbf{x}_k)$ , which weights the force of a particle at  $\mathbf{X}_m^i$  on the grid node located by  $\mathbf{x}_k$ .

The particle drag force is the sum of contributions from the fluid pressure gradient in the  $k^{th}$  cell and drag due to the relative velocity between the solid and fluid phases

$$\mathbf{F}_d^{i \in k, m} = -\nabla P_f(\mathbf{x}_k) \nu_m + \beta_m^k \frac{\nu_m}{\epsilon_{sm}} (\mathbf{V}_f(\mathbf{X}_m^i) - \mathbf{V}_m^i) \quad (8)$$

where  $-\nabla P_f(\mathbf{x}_k)$  is the cell centered fluid pressure gradient,  $\nu_m$  is the volume of the  $m^{th}$  solid phase particle,  $\epsilon_{sm}$  is the  $m^{th}$  solid phase volume fraction,  $\beta_m^k$  is the momentum

exchange coefficient for all  $m^{th}$  solids residing in the  $k^{th}$  cell, and  $\mathbf{V}_f(\mathbf{X}_m^i)$  is the interpolated mean fluid velocity at the particle location. Combining (7) and (8), the momentum exchange between the fluid and  $m^{th}$  solid phase becomes:

$$\mathbf{I}_{fm}^k = -\epsilon_{sm} \nabla P_f(\mathbf{x}_k) + \frac{1}{\nu_k} \sum_{i=1}^{N_m} \beta_m^k \frac{\nu_m}{\epsilon_{sm}} (\mathbf{V}_f(\mathbf{X}_m^i) - \mathbf{V}_m^i) K(\mathbf{X}_m^i, \mathbf{x}_k) \quad (9)$$

$\beta_m^k$  is calculated using the model outlined in (Gidaspow, 1994). The expression for the exchange term is dependent on the volume fraction of the fluid in the cell

$$\beta_m^k = \begin{cases} 150 \frac{(1-\epsilon_{sm})^2 \eta_f}{\epsilon(d_m^k)^2} + 1.75 \frac{\rho_f |\mathbf{V}_f(\mathbf{X}_m^i) - \mathbf{V}_m^i| \epsilon_s}{d_m^k}, & \text{if } \epsilon_f < 0.8 \\ 0.75 C_D \frac{\epsilon_f |\mathbf{V}_f(\mathbf{X}_m^i) - \mathbf{V}_m^i|}{d_m^k} \epsilon^{-2.65}, & \text{if } \epsilon_f > 0.8 \end{cases} \quad (10)$$

$$(11)$$

Thus, this momentum exchange scale factor is a function of the solid and fluid phase properties (including the fluid viscosity  $\eta_f$ ), the relative average velocities between the solid and fluid phases, and the drag coefficient  $C_D^k$ , which itself is a function of the cell's particle Reynolds number  $Re^k$ :

$$C_D = \begin{cases} \frac{24}{Re^k} (1 + 0.15(Re^k)^{0.687}), & \text{if } Re^k < 1000 \\ 0.44, & \text{if } Re^k > 1000 \end{cases} \quad (12)$$

This correlation between the drag coefficient and the Reynolds number works to reproduce the standard drag curve where the drag coefficient for a sphere is inversely proportional to the particle Reynolds number when  $Re < 1000$ , then becoming more or less constant prior to a critical Reynolds number where the drag coefficient decreases abruptly (e.g., Bird (1960)). These expressions are derived from a particular case of particle-fluid flow where the total pressure drop in the expression of momentum conservation is experienced in both phases.

### 2.1.1 Coarse Graining

To relate the resolved dynamics of individual particles to macroscopic flow properties we employ coarse graining techniques (CG). CG is a computational tool to derive continuous fields from discrete data. It has been employed in numerical studies to derive continuous fields of quantities like density, velocity, and stresses within the granular system (e.g. Fullard et al. (2019); Breard et al. (2022)). Detailed information on the CG technique used in this study can be found in Breard et al. (2020).

The CG method assumes that momentum is distributed through the system via non-instantaneous contacts between particles, whose contact area can be modeled as a contact point: particles are considered soft (i.e. collisions are not instantaneous) but hard enough such that particle deflections can be approximated to a point (Weinhart et al., 2013). Our CG methods uses a peaked Gaussian function that is convolved with microscopic properties, effectively performing spatial smoothing with a width equal to  $0.75d$ , where  $d$  is the monodisperse particle diameter. Convolved particle mass and momentum are used to satisfy conservation of momentum and to derive a bulk stress tensor that is the sum of kinetic and contact stresses

$$\overline{\overline{\sigma}} = \overline{\overline{\sigma^k}} + \overline{\overline{\sigma^c}} \quad (13)$$

In this way, stresses are broken down into contributions that are a function of particle velocity fluctuations, i.e.,  $\overline{\overline{\sigma^k}}$ , and contributions that are a function of the contact forces between particles, i.e.,  $\overline{\overline{\sigma^c}}$ . From this macroscopic description of the stress fields we can derive scalar parameters that will become important in subsequent scaling analyses (Section 2.1.2).

The solids pressure is defined by the trace of the total stress tensor

$$P_s = \frac{1}{3} tr(\overline{\overline{\sigma}}) \quad (14)$$

Similarly, the trace of the kinetic stress tensor gives the granular temperature under an isotropic assumption

$$T = \frac{1}{3\rho} \text{tr}(\overline{\sigma^k}) \quad (15)$$

Granular temperature is a parameter that is derived from kinetic theory applied to granular systems (Lun et al., 1984). This parameter captures the squared average fluctuating particle velocity, providing a measure of the fluctuating component of kinetic energy in the system. Anisotropic granular temperature estimates may be defined via the corresponding positions in the main diagonal of the kinetic stress tensor  $T_i = \overline{\sigma^k}_{i,i}/\rho$ .

We apply the plain strain assumption when calculating the deviatoric stress tensor

$$\sigma^D = \sigma^{2d} - \frac{1}{2} \text{tr}(\sigma^{2d}) \quad (16)$$

where  $\sigma^{2d}$  is the 2D stress tensor composed of the x (stream-wise) and y (bed-normal) components of the total stress tensor  $\sigma$ . From this we calculate the magnitude of shear stresses as

$$|\sigma^D| = \sqrt{\frac{1}{2} \sigma_{ij}^D \sigma_{ij}^D} \quad (17)$$

where repeated indices imply summation. Similarly, we can define the ‘magnitude’ of the shear-rate from the averaged (in the span-wise z-direction) particle velocity and 2D shear-rate tensor

$$\dot{\gamma} = |\dot{\gamma}^D| = \sqrt{\frac{1}{2} \dot{\gamma}_{ij}^D \dot{\gamma}_{ij}^D} \quad (18)$$

where  $\dot{\gamma}^D$  represents the domain averaged shear-rate deviator.

### 2.1.2 Scaling Parameters

The apparent coefficient of friction, or the ratio of shear to normal stresses, is defined as

$$\mu = \frac{|\sigma_{xy}|}{P_s} \quad (19)$$

where  $|\sigma_{xy}|$  is the domain integrated shear stress. This parameter follows, under certain conditions, a local rheologic assumption  $\mu(I)$ , stating flow is controlled by the local scaled shear-rate, known as the inertial number (MiDi, 2004):

$$I = \frac{\dot{\gamma}d}{\sqrt{P_s/\rho_s}} \quad (20)$$

This quantity can be seen as a ratio of the microscopic timescale for particle rearrangement under a confining pressure, and the timescale for macroscopic deformation as a granular bed is sheared (MiDi, 2004; Cruz et al., 2005; Forterre & Pouliquen, 2008). The  $\mu(I)$  scaling has been extended to include dense granular suspensions, taking the form  $\mu(I, I_v)$ , where

$$I_v = \frac{\eta_f \dot{\gamma}}{P_s} \quad (21)$$

This viscous inertial number can be written as a function of the inertial number and the stokes number  $I_v = I^2/St$  where

$$St = \frac{\dot{\gamma}d^2\rho_s}{\eta_f} \quad (22)$$

A scaling law unifying  $I$  and  $I_v$  was introduced by Trulsson et al. (2012) and written as the modified inertial number  $I_m$  by Amarsid et al. (2017):

$$I_m = (\alpha I_v + I^2)^{1/2} = I \left( \frac{\alpha}{St} + 1 \right)^{1/2} \quad (23)$$

where  $\alpha$  is a constant fitting parameter typically of order 1 that, here, will take the value of 2 after Amarsid et al. (2017). When  $St \rightarrow 0$ , time scales are dictated by viscous forcing, thus  $I_m$  is dominated by the viscous number  $I_v$ . Conversely, when particles gain inertia, and  $St \rightarrow \infty$ ,  $I_m$  reduces to  $I$ , signifying that dry granular processes control the system.

## 2.2 Experimental Setup

We perform two classes of experimental configurations: monodisperse plane shear and monodisperse inclined slope flows. Table 1 provides a summary of experimental parameters.

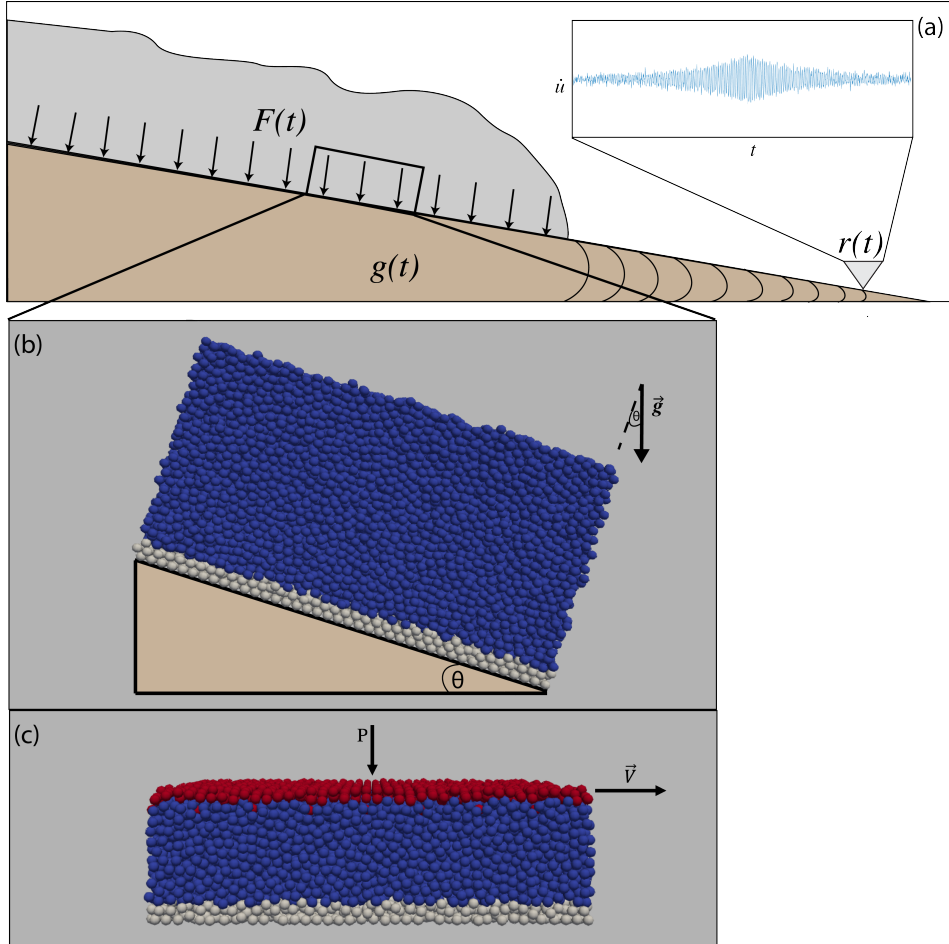


**Figure 1.** (a) Cartoon depicting radiation of elastic energy to receiver via forces exerted by the flow on the substrate. (b-c) Renderings of numerical experiment configurations addressing the unit problem of bed forces exerted by granular flows: (b) inclined slope flow where gravity is rotated by an angle  $\theta$  to simulate gravitational forces on a slope; (c) plane-shear configuration, where red particles act as a coherent plate, imposing a constant confining pressure and translational velocity on the blue particles. Gray particles on the bottom of the Y-Z plane act as a static rough and frictional ‘force plate’.

In plane shear configurations, a bed of particles is confined between two plates made frictional and bumpy, being composed of particles that comprise the bed (Fig. 1(b-c)):

the lower plate is made static and acts as a force plate, with an RMS surface roughness  $S_q \approx 0.6d$  (Supporting Information S1), recording particle forces (see Section 2.3); the top plate imposes a constant confining pressure and translational velocity, shearing the bed of grains and initiating flow. We keep a constant confining pressure of 2000  $Pa$ , allowing the height of the bed to evolve due to Reynolds dilation. The relatively low confining pressure, compared to meter scale geophysical flows, will have an effect on the inertial number reached at a given shear-rate (see denominator of Eq. 20). Nevertheless the physical processes at a given flow state described by the inertial number should remain the same. Periodic boundary conditions are imposed in the stream (x) and span-wise (z) directions, with both directions having dimensions equal to  $40d$ . In this configuration, we conduct two categories of experiments, pure granular flows (particles sheared in a vacuum) and flows submerged in two types of fluids: one with a density of  $1000 \text{ kg/m}^3$  and viscosity  $8.90 \times 10^{-4} \text{ Pa s}$ , and a more viscous liquid with the same density and a viscosity of  $0.01 \text{ Pa s}$ . The more viscous liquid was chosen to be an order of magnitude greater than water due to the viscosity of sediment-laden water in debris flow mixtures being 10 to 100 times greater than water (Iverson, 1997). Within these two categories (i.e. fluid submerged and dry granular flow), we run two sets of experiments, changing the bed composition from a monodisperse composition of  $500 \text{ }\mu\text{m}$  to a composition of  $5 \text{ mm}$  particles, while keeping the density constant at  $1050 \text{ kg/m}^3$ . This density value provide a slight negative buoyancy in the presence of the interstitial fluid, and is motivated by the density of volcanic tephra (Shipley & Sarna-Wojcicki, 1993). We vary the top plate velocity such that the experiments span global shear-rates from  $10^{-2}$ – $10^3 \text{ Hz}$ , developing creeping to collisional granular flows. Particle friction is held constant across the experiments at  $\mu_p = 0.53$ . See Supporting Information movie S1 for an example of plane-shear simulations in the quasi-static, intermediate, and collisional regimes described by the inertial number ( $I \sim 10^{-3}$ ,  $I \sim 10^{-2}$ , and  $I \sim 10^{-1}$ , respectively).

Inclined plane experimental configurations are conducted similarly, being composed of monodisperse beds placed on top of a frictional and bumpy (force) plate. The bed of particles is first allowed to settle under gravity on a horizontal plane. Then, the gravity vector is rotated to an angle  $\theta$  such that  $\theta > \theta_s$ , where  $\theta_s$  is the angle of repose, and the configuration is destabilized. After bed failure, the gravity vector is either rotated to greater values, or decreased below the angle of repose dictated by particle friction, utilizing the hysteretic nature of granular materials (Pouliquen, 1999). In this way, inclined flow experiments reach shear-rates from  $\sim 10^{-1}$ – $10^2 \text{ Hz}$ . In these configurations, we maintain a minimum bed height of  $20d$ , avoiding scale effects for thin flows (Pouliquen, 1999).

**Table 1.** Summary of simulation parameters.

<i>parameter</i>	<i>variable</i>	<i>value</i>
<b>Solid Parameters</b>		
diameter <sup>1</sup> [m]	$d$	0.005, 0.0005
density [ $kg\ m^{-3}$ ]	$\rho_s$	1050
elastic coeff. [ $Pa\ m$ ]	$k_n$	$(2 \times 10^8)d$
angle of repose [ $^\circ$ ]	$\theta_s$	$\approx 20$
particle friction coeff.	$\mu_p$	0.53
restitution coeff.	$e_n$	0.6
<b>Fluid Parameters</b>		
density [ $kg\ m^{-3}$ ]	$\rho_f$	1000
viscosity <sup>1,2</sup> [ $Pa\ s$ ]	$\eta_f$	$8.9 \times 10^{-4}$ , $10^{-2}$
<b>Experimental Parameters</b>		
domain size [m]	$X \times Y \times Z$	$40d \times \geq 20d \times 40d$
confining pressure <sup>3</sup> [ $Pa$ ]	$P_p$	2000
top plate velocities <sup>1,3</sup> [ $ms^{-1}$ ]	$V_p$	0.0001 – 16
inclination angle <sup>1,4</sup> [ $^\circ$ ]	$\theta$	20.5 – 28
<b>Numerical Parameters</b>		
DEM solver timestep [s]	$dt_s$	$\frac{\pi}{50} \left( \frac{k_n}{m_s} - \frac{\eta_m^2}{4m_s^2} \right)^{-1/2}$
fluid solver timestep [s]	$dt_f$	$(2 \times 10^{-2})d$

<sup>1</sup>Parameter takes on one of the values listed for a single simulation<sup>2</sup>Parameter relevant when interstitial fluid is present<sup>3</sup>Parameter for plane-shear configuration<sup>4</sup>Parameter for inclined-plane flows

### 2.3 Wall Analyses

To link macroscopic flow properties to bed forcing, we record all contact forces with the rough static plate located at the base of the experimental configuration. In this way, the bottom plate acts as a force plate. We shear the bed of grains until the system reaches a steadystate (see Supporting Information Section S2). We record forces at this bottom boundary with a frequency of 100 kHz across all simulations. The particle forces are summed across the entire plate, acknowledging that the frequency of this forcing is a function of the size of the numerical force plate (Iverson, 1997; Jalali et al., 2006): decreasing the area in which particle forces are summed increases the frequency of forcing by the factor at which the plate dimensions are reduced. From these plate measurements, we calculate the power spectral density (PSD)

$$P(f) = \frac{N}{\Delta f} |\tilde{F}(f)|^2 \quad (24)$$

where  $\tilde{F}(f)$  is the Fourier transform of the total forcing time-series on the lower plate boundary,  $N$  is the number of discrete observations (length of the time-series), and  $\Delta f$  is the sampling frequency. Arran et al. (2021) use the PSD as a measure of the squared

fluctuating force. Similarly, we express the fluctuating force as an integrated PSD and normalize it by the time averaged force exerted on the bottom plate, squared

$$\Lambda = \frac{\int_{f_{low}}^{f_p} P(f) df}{\langle F(t) \rangle^2} \quad (25)$$

where the lower bounds of integration is a function of particle size, with  $f_{low}$  ranging from 10 Hz for experiments with 500  $\mu m$  particles and 1 Hz for 5  $mm$  particles. The upper bounds is similarly a function of particle-scale parameters:

$$f_p = \tau_p^{-1} = \left( \frac{d}{\sqrt{k_n / \rho_s d}} \right) \quad (26)$$

where  $\tau_p$  is the timescale for particle deformation, according to stiffness, size, and density of the particle. Effectively, (25) allows us to compare force fluctuations across a wide frequency band ( $f \in [0, \min(f_p, f_{ny})]$ , where  $f_{ny} = 50$  kHz), and runs with variable particles sizes. Normalization helps encapsulating any magnitude effects that correspond to the bed's weight as well as the momentum transferred from impacts that are fundamentally a function of particle size (Tsuji et al., 1992; Yohannes et al., 2012). The amplitude spectrum of the force-plate time series is also used to calculate the mean frequency of the forcing (Vinningland et al., 2007; Farin et al., 2015)

$$\bar{f} = \sum \frac{\tilde{A}[f_i] f_i}{\sum \tilde{A}[f_i]} \quad (27)$$

where  $\tilde{A}$  is the discrete amplitude spectrum. Forces and velocities at the bed are used to calculate parameters described in Sections 2.1.1 and 2.1.2. The effective wall coefficient of friction  $\mu_w$  is the ratio of the time averaged sum of basal forces in the stream-wise and plate-normal directions (Artoni & Richard, 2015)

$$\mu_w = \frac{\langle \sum F_x \rangle}{\langle \sum F_y \rangle} \quad (28)$$

Similarly, we compare the CG'd granular temperature to the granular temperature at the wall, defined as the time and spatially averaged mean squared velocity fluctuation of particles in contact with the bottom plate (thus, impact velocities)

$$T_w^i = \left\langle (V_i - \langle V_i \rangle)^2 \right\rangle \quad (29)$$

Note, as with all wall parameters, uncertainty increases with shear-rate, as the total number of particles in contact with the bottom plate at write-out decreases.

### 3 Results

#### 3.1 Granular Rheology

##### 3.1.1 Effective friction and particle concentration

The rheology of pure granular flows, under disparate shear conditions, is well established, with empirical constitutive laws taking the form  $\mu(I)$  and  $\Phi(I)$  (Jop et al., 2006; Amarsid et al., 2017). Utilizing CG techniques described in Section 2.1.1, we have derived bed averaged fields for the stress tensor and solids volume concentration, recovering these scaling relationships for monodisperse flows with and without an interstitial fluid phase (Fig. 2). Further, we have plotted 12 free-surface sloped flow experiments to compare against classical couette-style flows. In Fig. 2a,b, we identify four regimes spanned by the numerical flows. First, a velocity weakening regime when  $I < 10^{-3}$  (similarly in  $I_m$  space in Fig. 2b), reflecting non-monotonic behavior that is posited to arise due to endogenous noise generated in low shear conditions (DeGiuli & Wyart, 2017). When  $10^{-3} < I < 10^{-2}$ , the friction coefficient maintains a relatively constant value, exhibiting rate-independence. This rate-independence has been referred to as the quasi-static regime (MiDi, 2004; Breard et al., 2020). The friction coefficient begins to experience



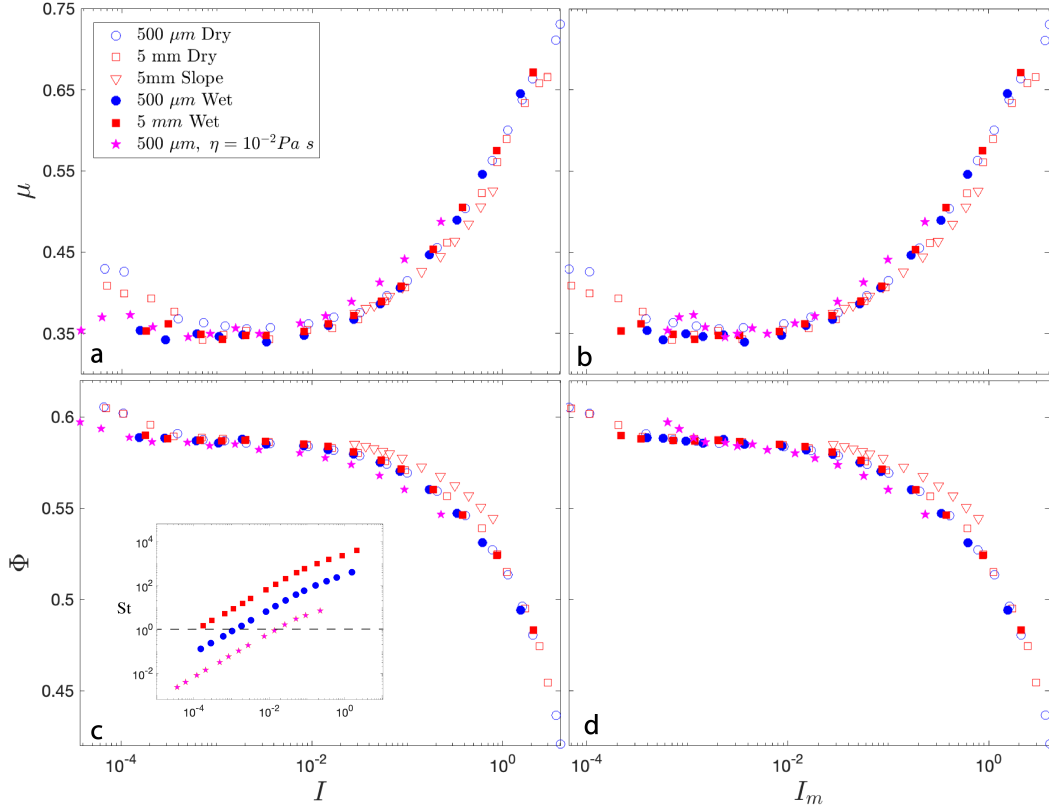


**Figure 2.**  $\mu(I)$  (a) and  $\Phi(I)$  (c) rheology with comparisons to  $\mu(I_m)$  (b) and  $\Phi(I_m)$  (d). Inset shows Stokes number vs  $I$  for each experimental run in the presence of an ambient fluid, with dashed line signifying when viscous forcing causes  $I_m$  to diverge from  $I$ .

rate dependence as  $I > 10^{-2}$ . This regime has previously been identified as the intermediate regime, when the bed of particles behave phenomenologically much like a liquid; the bed of particles does not support itself under shear loads, and particles remain in prolonged contact with one another, forming an evolving contact (force-chain) network that rotates, breaks, and reforms itself in time (Majmudar & Behringer, 2005; Forterre & Pouliquen, 2008). Finally, in the limit when  $I > 10^{-1}$ , the flow enters into a collisional limit, where the bed dilates greatly, prolonged contacts are reduced, with binary particle collisions taking the role of the primary mechanism for momentum transfer (MiDi, 2004; Cruz et al., 2005; Forterre & Pouliquen, 2008). Fig. 2 depicts both the dry inertial number and the modified inertial number on the abscissa (Fig. 2a,c and Fig. 2b,d, respectively). When the viscous term in (23) becomes important, i.e. when  $St \sim 10^{-1}$  (Fig. 2, inset), data points are shifted to the right when plotted with the modified inertial number  $I_m$  (Fig. 2b,d). This shift illustrates  $I_m$  accounting for viscous forces at low Stokes numbers, speaking to the added viscous-inertial rheologic effects that arise due to viscous shear when the particle response time is much lower than the characteristic flow time.

To begin linking bulk (CG'd) rheology to wall-bed interactions we can compare Fig. 2b to the effective wall friction on the bottom boundary,  $\mu_w$ , as defined in (28) (Fig. 3). The effective wall friction scales very similarly to the bed-averaged friction coefficient, but with much more spread; apparent master curves for each experimental configuration arise, with collapse to these curves being a function of the presence of a interstitial fluid (and its viscosity), as well as the experimental setup (i.e., shear cell or inclined slope

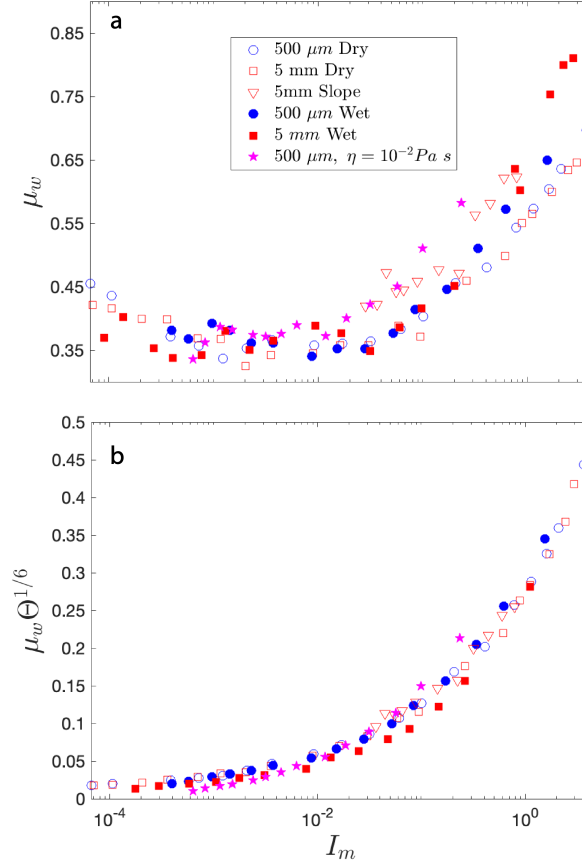


**Figure 3.** Wall friction as a function of  $I_m$  (a) and rescaled by non-dimensional granular temperature  $\Theta$  raised to the  $1/6$  (b).

flow). Kim and Kamrin (2020) suggest that the friction coefficient rescaled by a non-dimensional granular temperature ( $\Theta = \rho_s T / P_s$ ) helps collapse variability across flow configurations. Following this, Fig 3b depicts their suggested scaling, showing variability in wall stresses being effectively balanced by bulk granular temperature.

### 3.1.2 Granular temperature

In conjunction with measures of the ratio of stresses and concentration, we can examine granular temperature, using it to help classify our experimental flows. Fig. 4 depicts non-dimensional isotropic granular temperature  $\Theta$  as a function of  $I$  and  $I_m$ , both of the entire bed and of particles one grain diameter from the bottom ‘force plate’ (Fig. 4a-b and 4c-d, respectively). Again, we express these measures as functions of  $I$  (Fig. 4a,c) and the modified inertial number  $I_m$  (Fig. 4b,d). Non-dimensional granular temperature appears to scale well with  $I$ , independent of particle size, the presence of a liquid phase, or changes in flow configuration. Nevertheless, Fig. 4b,d show that when viscous stresses cause  $I_m$  to diverge from the dry inertial number, data fall away from the collapsed master curve. This, in addition to the fact that  $I_m$  has a marginal effect on data derived from experiments submerged in a liquid — suggesting viscous shear stresses are not playing a large role in changing the dense granular rheology — leads us to report remaining data only in terms of the dry inertial number. We will explore the implications of this in the discussion.

Granular temperature is commonly assumed to be isotropic in many approaches that utilize kinetic theory applied to rapid granular flows (e.g., (Johnson & Jackson, 1987; Syamlal et al., 1993; Berzi et al., 2020). Nevertheless, the anisotropic nature of this fluctuating energy has been observed rather early in the theory’s lifespan (e.g., Campbell (1989)). We plot the ratio of the stream-wise granular temperature to the component normal to the bottom plate, giving insight into how momentum is communicated and advected through the system (Campbell, 2006) (Fig. 4e-f). In general terms, as  $I < 10^{-3}$ , the y-component of granular temperature overtakes the stream-wise component. Alternatively, as  $I \rightarrow 1$ , the stream-wise component exceeds the vertical component (Fig. 4e). Note that viscosity of the interstitial fluid phase plays a large role in this behavior, with the stream-wise component overtaking the plate-normal component when  $I \sim 0.3$ . Velocity fluctuations at the wall show a strong bias in the x-direction across all experiments, independent of  $I$  (Fig. 4f). This bias, regardless of  $I$  is due to the concentrated nature of the flows and vanishing velocity gradients near the base of the flow. Regardless, wall-averaged granular temperature follows a similar trend with the viscous interstitial fluid simulations diverging from the bulk of the experiments, further suggesting the degree of anisotropy is a strong function of interstitial fluid viscosity.

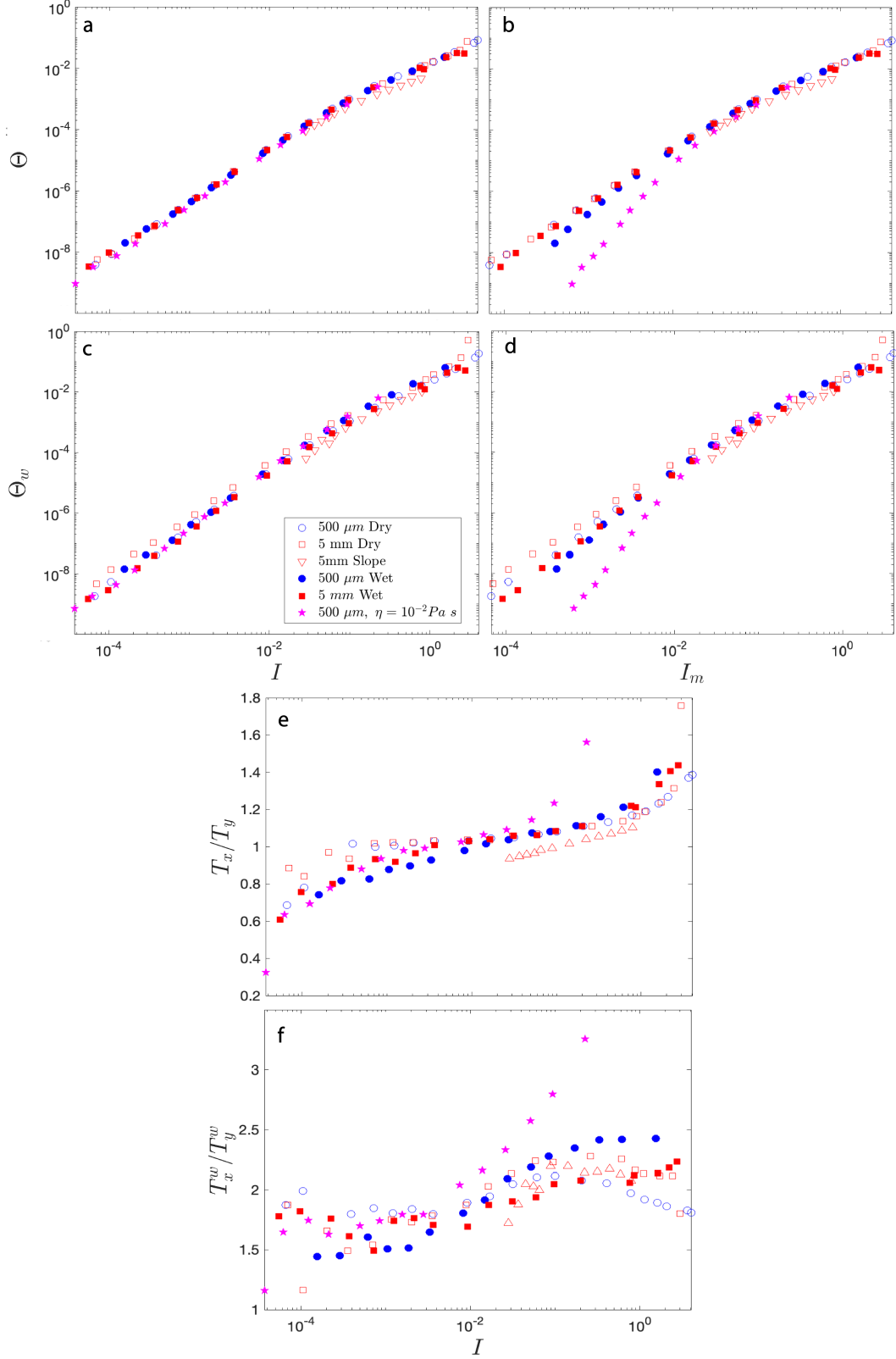


**Figure 4.** Coarse grained (CG) non-dimensional granular temperature (a-b) and wall averaged at the bed-plate interface (c-d), functions of  $I$  (a,c) and  $I_m$  (b,d). (e-f) Ratio of stream-wise and spanwise granular temperature vs  $I$ : (e) CG'd granular temperature and (f) wall averaged.

### 3.2 Wall forces

Wall forces are how geophysical mass flows effectively communicate flow momentum to the earth. Encoded in this exchange is an energy cascade that converts flow driving energy to shear work, which is dissipated through particles interacting with their neighbors and the boundary, and ultimately through frictional heating (Iverson, 1997). To this end, we will examine how forces fluctuate on the scale of an experimental flow’s footprint — the bottom static plate acting as a force plate where contact forces are recorded — with the goal to relate these back to macroscopic rheologic behavior.

Fig. 5 depicts time series of the sum of forces acting on the bottom plate as well as the power spectral density (PSD) of these forces. The character of the time series is not strongly dependent on the experimental configuration, but rather the inertial number (shear-rate). As  $I$  increases, the time series transitions from unsteady behavior (Fig 5a) to a noisy process with a well defined D.C. component (Fig 5g). Similar behavior is observed in the stream-wise sum of forces  $\Sigma F_{yx}$ . The PSD is a measure of how the signal’s power is binned in frequency space, and we can use this to examine how the organization of forcing energy evolves with increasing shear. The character of the power spectra changes drastically with  $I$ ; when  $I < 10^{-3}$ , the spectra decays near linearly in log-log space, following a power law scaling that closely follows  $f^{-2/3}$  (Fig. 5b); when  $I \sim 10^{-2}$ , the spectra begins to lift, though the decay remains monotonic (Fig. 5d); as  $I$  approaches and exceeds  $10^{-1}$  — often taken as the transition from intermediate to collisional flow (Forterre & Pouliquen, 2008) — the spectra continues to flatten (Fig. 5f), approaching a near flat response that is finally actualized when  $I \sim 1$  (Fig. 5h). Note the spectral hump that appears when  $I \sim 10^{-4}$  and (to a lesser extent)  $I \sim 10^{-2}$  (Fig. 5b,d). This shifts to the right as the particle size decreases, suggesting this peak in spectral amplitude is an emergent from particle-scale properties.

Using (27) we analyze how the frequency content of the time series changes with  $I$  (Fig. 5i-j). Fig. 5i shows the unscaled mean frequency, showcasing how the mean frequency is a strong function of particle size and inertial number. Scaling mean frequency with the characteristic particle deformation time  $\tau_p$  collapses the data in log-log space, with only slight dispersion from the master curve observed when experiments are submerged in a viscous fluid, and  $I > 10^{-2}$  (Fig. 5j). Moreover, the concavity of the curve shows a distinct change as the inertial number approaches, and becomes greater than,  $10^{-2}$ , providing evidence that phenomenological changes in bed rheology occurring at intermediate  $I$  may be effectively captured in bed forces.

This study is in part motivated by the ability of granular flows to radiate elastic energy that can be observed in real-time in the form of seismic signals (see Allstadt et al., 2018 for a review on signals used to observe geophysical mass flows). A static forcing will not generate an observable signal (i.e., if one merely stands still next to a seismometer, no ground movement will be recorded), thus we are concerned with the basal (wall) force fluctuations in-time. To this end, we plot the non-dimensional integral of experimental PSDs — as defined in (25) — allowing a glimpse at how the variance in wall-forcing time-series, and the binning of power in frequency space, changes with increasing shear-rate for a given experimental configuration (Fig. 6a). We observe that  $\Lambda$  is a strong function of inertial number, and correspondingly, a function of  $\Theta$  (Fig. 6b). This shows that the strong relationship between fluctuating energy, as described by granular temperature and  $I$  (see Fig. 4a) is maintained as forces are communicated to the wall boundary. Fig. 6a depicts a shift in the relationship between  $\Lambda$  and  $I$  as  $I \rightarrow 10^{-1}$ ; when  $I < 10^{-1}$   $\Lambda \sim I$ , but as  $I$  approaches  $10^{-1}$ ,  $\Lambda$  changes from an increasing function of  $I$ , to then decrease with  $I$  until  $I > 10^{-1}$ , henceforth scaling with  $I^{0.6}$ . Note that the power at which  $\Lambda$  scales with  $I$  changes with the frequency range the PSD is integrated over; integrating only over the high frequencies yields power law behavior where the exponent is greater than one (Arran et al., 2021) (see Supporting Information S3). This change from a monotonic increasing function, to a slight decrease before increasing again

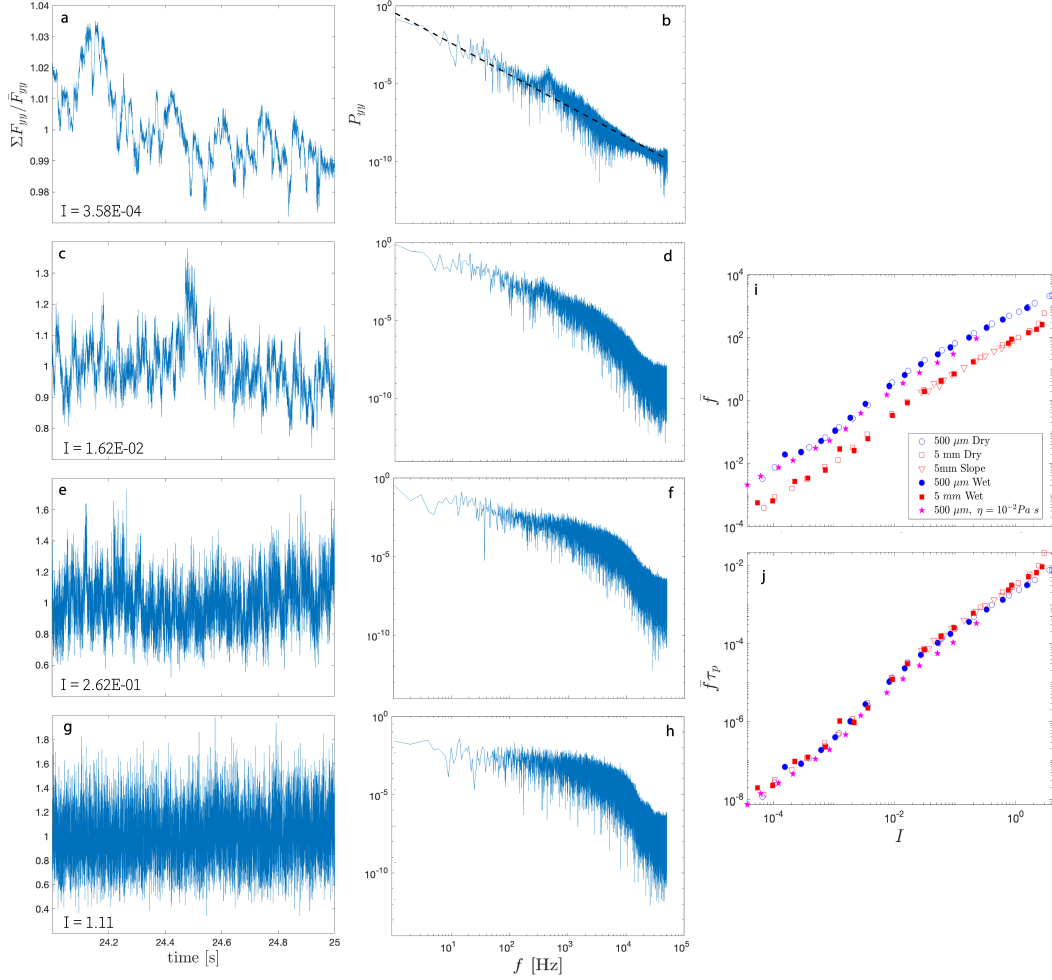


**Figure 5.** Time series of the normalized sum of normal forces (a, c, e, g) and the power spectral density of sum of normal forces (b, d, f, h) exerted onto the bottom plate during dry shear cell experiments with bulk inertial numbers labeled  $I < 10^{-3}$  (a-b),  $I \sim 10^{-2}$  (c-d),  $I \sim 10^{-1}$  (e-f), and  $I \sim 10^0$  (g-h). (b) Shows the log-linear power law decay that goes as  $f^{-2/3}$ . (i-j) Mean frequency of forces depicted in a-h, as defined in (27), versus dry inertial number, unscaled (i) and scaled (j) with the characteristic particle deformation time  $\tau_p = d/\sqrt{k_n/\rho_s d}$ .

with the independent variable, with a new power scaling, is reflected in the relationship between  $\Lambda$  and  $\Theta$  (Fig. 6b). Further, we find that  $\Lambda = F(\Phi)$ , with a strong shift in scaling behavior when  $\Phi \approx 0.57$  (Fig 6c). A similar relationship has been observed in flume experiments utilizing sediment-water mixtures (Piantini et al., 2023).

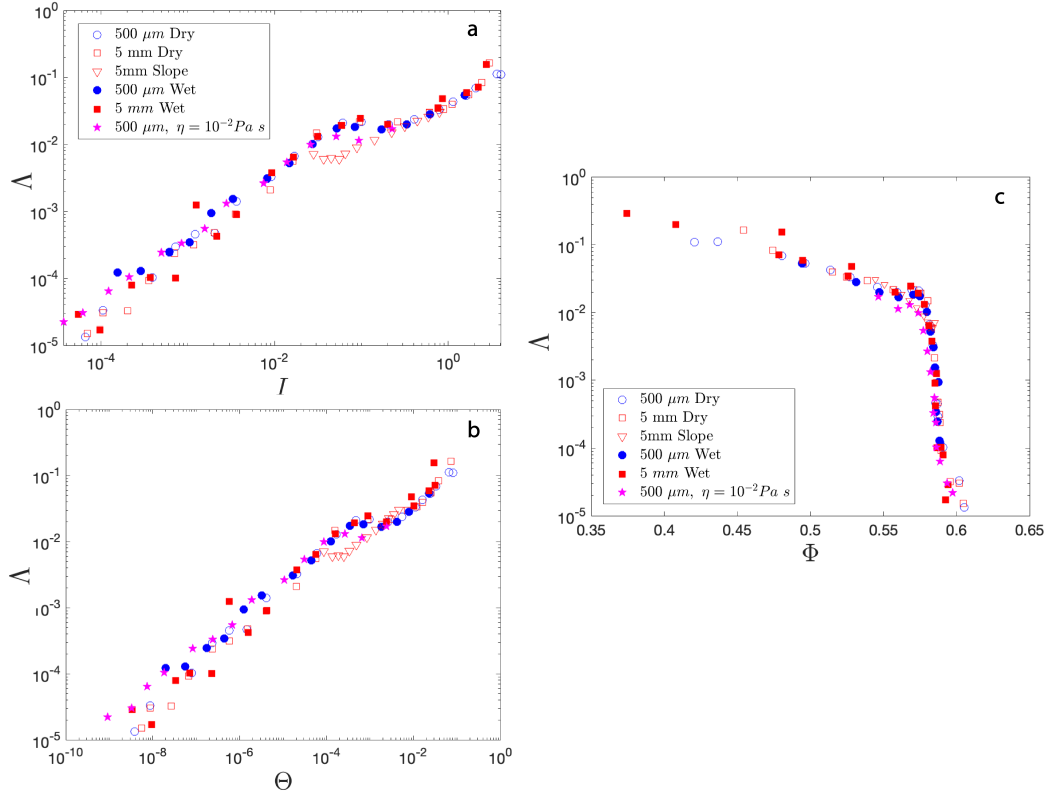


**Figure 6.** Non-dimensional force fluctuations as a function inertial  $I$  number for a given experiment (a), non-dimensional granular temperature  $\Theta$  (b), and solids fraction  $\Phi$  (c).  $\Lambda$  is strongly correlated with  $I$ , with distinct changes in scaling behavior that is dependent on  $I$ ; for  $I < 10^{-1}$ ,  $\Lambda \sim I$ ; for  $I > 10^{-1}$   $\Lambda \sim I^{0.6}$ . This correlation and marked shift in scaling of the forcing fluctuation is mirrored when plotted against  $\Theta$ .

## 4 Discussion

Geophysical surface flows are a complex phenomenon that pose challenges to life and property. Therefore, there is great need in the ability to deduce flow information from observation. The implications of results reported in this study are that boundary stresses can retain information about the macroscopic flow. This suggests that force plate data, as well as ground movement resulting from boundary forcing (i.e. seismic data), may be used to make statements about flow dynamics. Further, the discrete element methods employed in this study allow us to calculate granular temperature as a primary measure, from which a continuous field variable is derived. This allows us to look at the interplay between flow-averaged velocity fluctuations and flow driving shear.

### 4.1 Fluctuating energy generated through shear work, and enhancement of anisotropy through fluid-solid coupling

Granular temperature is an important measure of velocity fluctuations that has been used widely through kinetic theory treatments of granular flows. This temperature is traditionally used to infer pressure, shear stresses, and viscosity in high-energy, dilute systems (Lun et al., 1984; Johnson & Jackson, 1987). Granular temperature may play an important role in the enhanced runout of natural granular flows (e.g. Campbell (1989)). For example, granular temperature is observed to concentrate in dilute regions below dense



cores of high speed unidirectional flows, reducing the effective basal friction with increasing mass (Brodu et al., 2015). Granular temperature, as a measure of the fluctuating energy of a particle, is an integral part of the energy cascade inherent to granular flows as dissipative systems. In this cascade, flow driving forcing is converted into macroscopic kinetic energy, as described by the mean velocity, which in turn drives fluctuating velocities of individual grains. Velocity fluctuations lead to dissipative interactions, closing the cascade of energy loss to irrecoverable particle deformation and frictional heating (Campbell, 2006). Here, we report granular temperature as derived from the kinetic stress tensor (15), thus a continuous field derived from discrete particle velocity fluctuations.

In these experiments, granular temperature is produced through shear work and particle-particle interactions — rather than boundary layer effects resulting in wake structures contributing to kinetic energy fluctuations (Mehrabadi et al., 2015). Fig. 4b,d show that plotting  $\Theta$  as a function of  $I_m$  causes a move-out away from the master curve, with these data points corresponding to when  $St < 1$ . This shows that even when  $I_m$  becomes dominated by visco-inertial effects,  $\Theta$  is better parameterized by  $I$ . Regardless, Fig. 4e-f shows that the degree of anisotropy in temperature is enhanced by the presence of an interstitial viscous liquid. Anisotropy in granular temperature can be likened to a measure of a bias in the transmission of momentum, as well as how granular temperature is being produced, e.g., through particle-particle interactions or shear work and corresponding velocity gradients (Campbell, 2006). From the quasi-static to the intermediate regime ( $10^{-3} < I < 10^{-1}$ ), macroscopically defined granular temperature is roughly isotropic, suggesting that this variable is maintained through particle-particle interactions, leading to an equal partitioning of fluctuating energy in three dimensions. As  $I \rightarrow 10^{-1}$ , granular temperature becomes biased in the x direction, suggesting that temperature production becomes dominated by velocity fluctuations due to particles moving normal to the velocity gradient. As shear induced velocity gradients develop, random particle motion normal to the gradient can enhance the generation of granular temperature; this is known as the streaming effect. The streaming effect causes granular temperature to be biased in the shearing direction. Viscous forces contribute to particle-shearing. Therefore, the inertial number at which this bias occurs is a function of the presence of, and viscosity of, an interstitial liquid. The dry granular experiments are lacking these viscous shear contributions. Thus, the simulations involving a liquid phase reach anisotropic conditions at lower inertial numbers, compared to the simulations without a liquid phase (Fig. 4e-f). In the other limit, when  $I < 10^{-3}$ , granular temperature is biased in the direction normal to the bottom boundary. This correlates to the regime where  $\mu$  decreases with  $I$  (Fig. 2). With this correlation in mind, anisotropy at these low inertial numbers can be linked to particle reorganization; particles mount those that reside in layers lower and adjacent to them, sliding and falling back down under the force of the top plate’s confining pressure (DeGiuli & Wyart, 2017). Moreover, bed spanning force chains in this low inertial number regime are long lived, but susceptible to buckling events, causing motion normal to the shearing plane during slip events (Tordesillas et al., 2011). Individual contact forces further reflect this directional dependence on inertial number (Supporting Information S4).

The differences in the two modes of granular temperature production (particle-particle interactions or shear induced ‘heating’) can also be indicated through the relationship between granular temperature and inertial number. Fig. 4 shows a direct relationship between inertial number and granular temperature rescaled by the solids pressure and the particle density. Rescaling is required for all of simulations to collapse to a master curve. Without this scaling, the relationship between granular temperature and inertial number is controlled by the experimental setup: sloped flow simulations reach granular temperatures nearly an order of magnitude less than that of a shear cell experiments at an equivalent inertial number. We relate this decrease to the fact that the sloped flow simulations do not experience the same magnitude of shear. Nevertheless, as is the case

with rescaling the coarse grained shear-rate by the timescale of particle rearrangement (a function of the solids pressure), giving equivalent inertial numbers across experimental configurations, rescaling the granular temperature by the solids pressure accounts for the deviation observed in granular temperature. Thus, non-dimensional granular temperature can provide a link across not only various flow geometries (Kim & Kamrin, 2020) but granular matter under disparate confining pressures. This suggests that the solids pressure corrects for the lack of shear work provided to generate granular temperature in the free-surface simulations. This is important for evaluating bed forces as solids pressures may vary significantly in natural flows interacting with complex topography (Benage et al., 2016).

## 4.2 Basal forces record granular phase transitions

Previous laboratory experiments have constrained a correlation between  $I$  and an estimate of the variance in basal forces ( $\Lambda$ ) for inclined plane flows at high inertial numbers (i.e.,  $I > 10^{-1}$ ; Arran et al. (2021)). Here, we expand this by performing analysis that probes a wider range in inertial space, with  $I$  spanning from  $10^{-4}$ – $10^0$ . With this expansion, we are able to demarcate distinct flow regimes by correlating changes in  $\Lambda$  with macroscopic quantities derived from coarse-graining procedures.

Fig. 6 shows that there are distinct changes in the nature of how  $\Lambda$  scales with inertial number; in shear cell simulations, as  $I \rightarrow 10^{-1}$ ,  $\Lambda$  ceases its near constant increase with  $I$ , plateauing then dropping slightly just as  $I > 10^{-1}$ . This is, to an extent, mirrored by the inclined slope simulations:  $\Lambda$  stays relatively constant with increasing shear-rates when  $10^{-2} < I < 10^{-1}$ , then recovers the scaling behavior observed in the shear cell simulations. This shift is corroborated in Fig. 6c which depicts a critical value of  $\Phi$  after which  $\Lambda$  increases from a local minimum. This critical solids concentration has been touched on by others, suggesting its relation to a glass transition: when  $\Phi > 0.57$ , the packing fraction begins to inhibit strain (Zhang & Kamrin, 2017). This is analogous to a critical volume fraction that may define a glass transition in which kinetic properties of a liquid is diminished as it is undercooled and avoids crystallization (Cohen & Turnbull, 1959). Moreover, a similar critical value of  $\Phi$  is observed in dense suspensions, below which the rheology of the system is controlled by the Stokes number of the solids phase, and above which is a contact dominated regime that is rate-independent up to a critical shear-rate, where then the suspension rheology becomes rate-dependent (Ness & Sun, 2015).

The plateau in  $\Lambda$  that occurs at this glass-like transition (i.e. when  $\Phi \approx 0.57$ ) is accompanied by a decrease in the rate of change in the ratio of the magnitude of the (deviatoric) kinetic and total stresses (the sum of the kinetic and contact tensors); as  $I \rightarrow 10^{-1}$ ,  $|\sigma_k^D|/|\sigma^D|$  becomes concave, suggesting a decrease in the rate at which kinetic stresses balance out shear-work with increasing  $I$  (Fig. 7). At this state, the internal contact network is altered, with the density and length of force chains decreasing dramatically (Fig. 8). When  $I < 10^{-1}$ , high magnitude force chains (greater than two times the granular bed’s weight) propagate through the entirety of the domain (Fig 8a). When  $I \sim 10^{-1}$ , contact forces are still correlated in space, but they are not as abundant (Fig 8b). This behaviour can be further evidenced by the decrease in the average coordination number with  $I$  (Fig. 8b, inset). Thus, we suggest that shear work is consumed by the process of bed dilation, destroying aspects of the force chain network during the ‘phase’ transition from a contact dominated liquid-like granular phase, to a collisional gas-like flow. This processes effectively inserts itself into the dissipative cascade of flow driving energy being converted into particle-scale energy fluctuations (measured by the kinetic stress tensor), that is ultimately dissipated through irrecoverable deformation, frictional heating, and acoustic emissions (Siman-Tov & Brodsky, 2021).

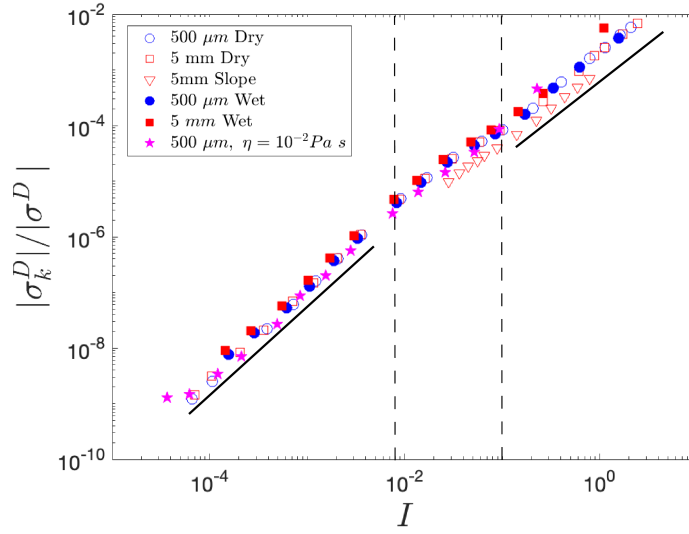


**Figure 7.** Ratio of the magnitude of deviatoric kinetic stress to the magnitude of total deviatoric stress ( $\sigma^D = \sigma_c^D + \sigma_k^D$ ) as a function of  $I$ . Vertical dashed lines demarcates when the rate of change with the increase in  $I$  decreases, transitioning from a log-log linear scaling that goes as  $I^{1.6}$  (solid line from  $10^{-4} < I < 10^{-2}$ ) to  $I^{1.4}$  (solid line from  $10^{-1} < I < 10^0$ ).

Fig. 9 summarizes our data with an annotated figure of  $\Lambda$  plotted over  $I$ . The first regime is spanned by  $I < 10^{-3}$ , and is characterized by many high magnitude, domain spanning, force chains (Fig. 9a). Rheologically, this regime is concomitant with a decrease in the coarse-grained apparent coefficient of friction with increasing shear-rates (Fig. 2a). This decrease in the stress state has been observed elsewhere and attributed to endogenous vibrations coaxing particles to slip as they are near failure (DeGiuli & Wyart, 2017). This is supported by the fact that granular temperature is dominant in the vertical direction, thus individual particle motion, ‘noise’, works to dilate the bed of grains, decreasing the number of particles in static contact. This likely works in tandem with top plate motion stretching and rotating the long-lived force chains in the system, causing them to buckle and the bed to dilate (Tordesillas et al., 2011). The power spectra of basal forces in this regime reflects power law scaling that is reminiscent of critical systems (Fig. 5a). Thus, we suggest that basal forces in this regime represent the diffusion of reordering events down to the base of the domain as shear-stresses generated by the top plate drive unsteady slip events (Cruz et al., 2005).  $\Lambda$  scaling shows higher degrees of dispersion about a general increasing log-linear trend, dependent on particle size. This is due to the sensitivity of our results to spectral resolution: the mean frequency of the bed forcing signal is a function of  $I$  (Fig. 5i-j), thus more energy is binned in lower frequencies with decreasing  $I$ . The lowest resolvable frequency is dictated by the length of the time-series and the sampling frequency ( $\Delta f = f_s/N$ ), as these do not change across simulations and particle size ( $f_s = 100$  kHz and  $N = 100000$ ). Thus, in this regime, particle size has a first order control on the frequency bands basal forcing power is relegated to, matching the fact that low inertial numbers signify when the time scale for particle rearrangements (function of particle size and confining pressure) dominates the kinematics of the system (MiDi, 2004).

The second regime is characterized by  $10^{-3} < I < 10^{-2}$  (Fig. 9b). Here, the bed experiences a relatively constant stress state in which increases in  $I$  does not lead to large changes in the bed averaged apparent friction (Fig. 2a). Basal forces develop a more defined DC offset (Fig. 5b).  $\Lambda$  scaling with  $I$  reflects this as the trend of  $\Lambda \sim$

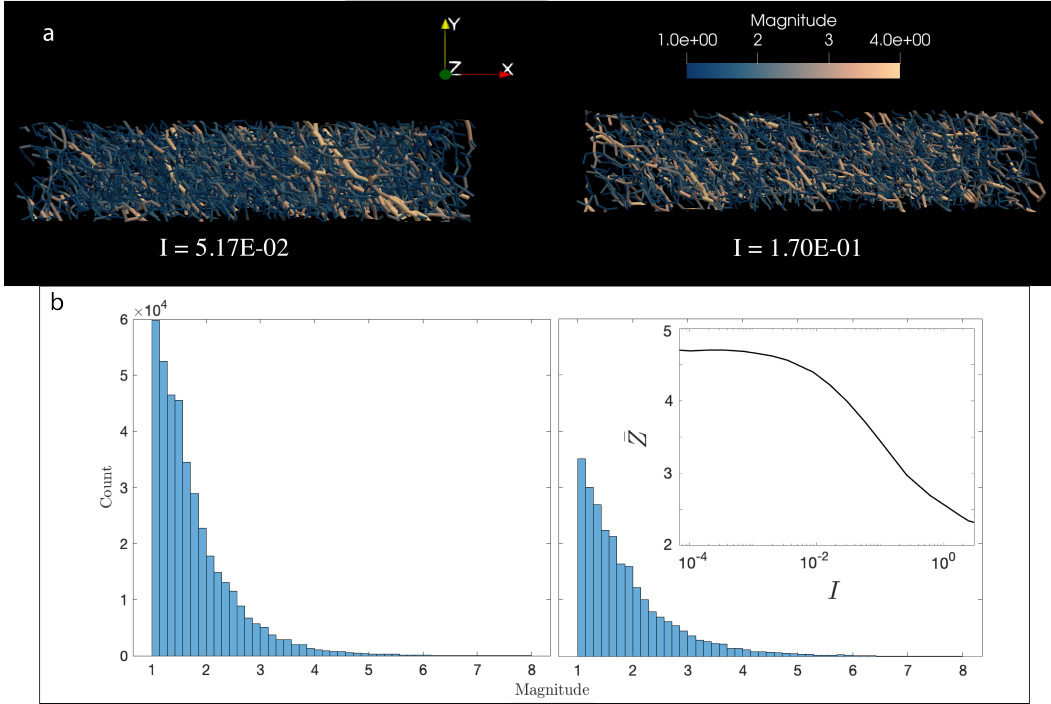


**Figure 8.** (a) Visualization of force chains whose magnitude is non-dimensionalized by the average contact force for shear cell experiments with  $I \sim 10^{-2}$  (left) and  $I \sim 10^{-1}$  (left). Here, each contacting pair of particles is represented by a tube whose color and radius is scaled by the contact force normalized by the bed’s weight. (b) Histograms of contact forces showing number of contacts binned via the non-dimensional magnitude. Inset: Time averaged coordination number  $\bar{Z}$  as a function of  $I$ .

$I$  continues well into this regime, and is accompanied by the collapse of data points from disparate particle size simulations onto a single curve; basal forcing in this regime is less controlled particle scale parameters, but instead by the global kinematics of the system represented by the inertial number. This intermediate regime marks the transition from quasi-static behaviour to continuous deformation of particles that remain in prolonged contact with one another. This is supported by the development of isotropic granular temperature, suggesting that energy fluctuations are controlled by those prolonged particle contacts (Campbell, 2006; Fig. 4e-f).

Increasing shear-rates leads to a transitional regime where  $10^{-2} < I < 10^{-1}$  (Fig. 9c). In this regime, the apparent coefficient of friction increases monotonically (Fig. 2a), granular temperature remains isotropic in the absence of a viscous interstitial fluid (Fig. 4e-f), and, most notably, the scaling of basal force fluctuations with  $I$  reaches a plateau and slightly decreases as  $I \rightarrow 10^{-1}$ . This transitional regime is reminiscent of latent heat of vaporization required to disrupt inter-molecular forces during the phase transition from liquid to gas. This analogy is carried further by the decrease in contact forces supporting forces well above the beds weight (Fig. 8). The plateau in  $\Lambda$  can be explained by the ratio of deviatoric kinetic stresses to total deviatoric stresses becoming concave, signifying a relative decrease in the rate of change of kinetic stresses balancing out shear-work and becoming converted into basal forcing fluctuations (Fig. 7). This regime is also characterized by the beginning of the dramatic decrease in solids concentration with  $I$  (Fig. 2c). Thus, we interpret this transitional regime as the point in which flow driving

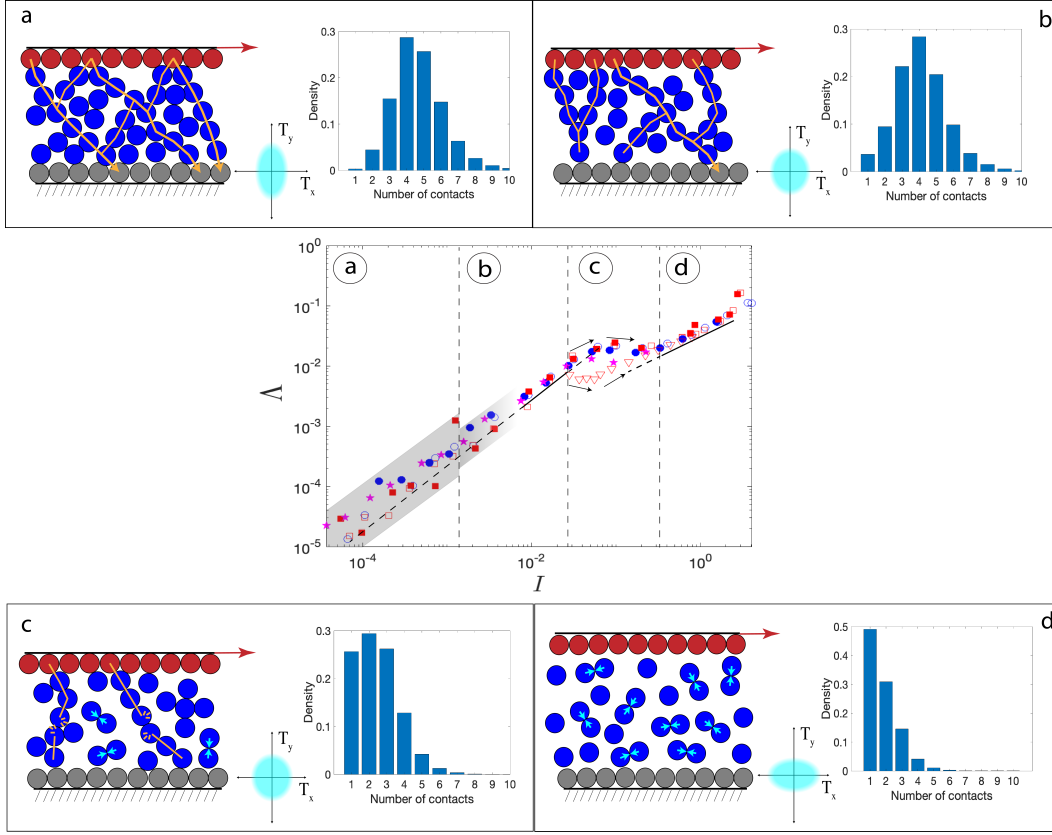


**Figure 9.** Annotated Fig. 6, highlighting four regimes spanned by  $\Delta$ , with bar charts showing the probability density of the number of contacts, and an axis representing the x and y components of granular temperature, where the cyan field qualitatively depicts the degree of anisotropy in that regime. (a) Force-chain dominated regime where  $\Delta \sim I$ . High magnitude domain spanning force chains cage particles; unsteady particle fluctuations, predominantly in the y-direction, disrupt the otherwise static architecture, weakening  $\mu$ . (b) Intermediate regime where linear log-log scaling persists and strengthens to the point of data as bed deformation becomes continuous. Coordination number decreases with rapid building and breaking of low magnitude force chains correlative to macroscopic deformation; granular temperature becomes isotropic. (c) Transitional regime analogous to a latent heat-energy required to break force chains; as shear energy is fed into the system the bed begins to dilate. Strong preparation dependence evidenced by dispersion in data between plane-shear and sloped flow (inverted triangles). Isotropic granular temperature drives the increase in binary particle collisions (depicted via cyan arrows) (d) Collisional regime where preparation effects no longer play a role, and  $\Delta \sim I^{0.6}$ . Granular temperature is biased in the x-direction and binary particle collisions are the dominant mode of particle-particle interactions.

energy is consumed by the dilation of the granular bed with increasing shear-work, thus affecting the energy cascade of flow energy being dissipated to the boundaries of the flow through particle-wall interactions. Importantly, this regime contains the lowest  $I$  values of the free surface inclined slope flows, and  $\Delta$  measured in these simulations are displaced from the magnitude of values recorded in the shear cell configurations, though the general trends are maintained.

The last regime spanned by our data is the gas-like the collisional regime (Fig. 9d). In the limit when  $I > 10^{-1}$ , basal forces becomes noise-like, with a flat spectral response across a wide band of frequencies (Fig 5h). Here, granular temperature becomes biased in the stream-wise direction, suggesting the development of kinetic energy fluctuations through collisions and particle movement in the direction of shear derived velocity gradients (Campbell, 2006; Fig. 4e-f). Basal forcing scaling shows a collapse across particle sizes and configurations to  $\Lambda \sim I^{0.6}$ . This change in scaling behavior is mirrored by the scaling of  $\Lambda$  with  $\Phi$ ; as  $\Phi > 0.57$  (exemplary of simulations with  $I > 10^{-1}$ ; Fig. 2c) the scaling curves kinks, and the rate at which  $\Lambda$  increases with decreasing solid concentration decreases. We denote this transition as a glass-like transition. It is notable that once this transition is crossed,  $\Lambda$  measured in the sloped flow configurations joins the scaling curve of the shear cell simulations, thus this transition suggests that as flow driving energy is used to dilate the flowing grains, preparation effects that occur near the packing fraction (e.g. Josserand et al. (2000)) no longer play a strong role in fluctuating forces recorded at the base of the flow. This relativity shows the partitioning of flow information between what is considered to the high frequency band, associated with uncorrelated particle impacts, and the relatively low frequencies that corresponding to correlated particle motion and bulk kinematics.

## 5 Conclusions

Here we have recorded basal forces generated during dry and submerged granular flow simulations — in plane shear and inclined slope flow configurations — with the aim to correlate these signals to descriptions of the flows derived from coarse-graining procedures. Utilizing both the rheologic and kinematic data from these simulations, we can describe four regimes that are effectively encoded in the forces exerted by the flow onto the simulated force plate (Fig. 9). The four regimes are: (I) a solid-like regime characterized by long-lived force chains structures, basal force measurements being controlled by particle-scale parameters (i.e. size and hardness), anisotropic granular temperature biased in the vertical axis, and decreases in the stress-state with increasing shear (velocity weakening); (II) an intermediate regime where the bed of particles deforms continuously, force chains build and break rapidly, basal forcing is less sensitive to our resolution allowing the data to collapse, and granular temperature becomes isotropic; (III) a transitional regime that showcases a disruption in the conversion of flow driving energy being converted to basal forcing, a dramatic decrease in solids concentration, and preparation dependence in how basal fluctuations scale with shear-rate increases; and finally (IV) a collisional regime marked by a noisy basal forcing signal, where force chains cannot be maintained, and data collapses in  $\Lambda(I)$  space. In summary, Fig. 9 suggests that basal tractions are well parameterized by kinematic quantities. This can lead to the development of sub-grid models to resolve basal tractions in large-scale geophysical flows.

We have shown that basal forces can encode detailed information about the dynamics of dry and submerged granular flows. This will prove useful in using boundary stresses as proxies for internal dynamics of real-scaled geophysical and industrial flows. Importantly, this effort provides a test bed that allows us to understand what rheologic and kinematic data can potentially be extracted from these signals. Future work can utilize this understanding when analyzing forcing signals from well instrumented debris-flow channels in natural deranges and large scale experiments (the reader is referred to McCoy et al. (2013); Allstadt et al. (2020)), as well as the development of sub-grid models for basal stresses. Moreover, our data provides a clue in how inverted basal tractions from seismic signals generated by debris flows may be used to elucidate dynamical and rheologic information about a given flow, providing another tool for probing these complex and dangerous phenomenon.



## 6 Open Research

The DEM-CFD code used to reproduce this data is publicly available at <https://mfix.netl.doe.gov>. Readers can find more information, and movie visualizations of example numerical experiments in the supporting information. Data used to produce figures can be accessed through the Zenodo repository: <https://doi.org/10.5281/zenodo.8436292>. The authors can provide more detailed information on numerical experiments and post-processing on request.

## Acknowledgments

Financial support to P.Z. and J.D. provided by NSF EAR grants 1926025 and 1949219. P.Z. was further supported by NASA award 80NSSC20K1773. E.C.P.B. was supported by UKRI with the NERC-IRF (NE/V014242/1). We thank University of Oregon’s High Performance Computing cluster Talapas for providing support and the infrastructure to produce the data. The authors would also like to thank the reviewers for their feedback and thoughtful comments that strengthened this effort.

## References

- Allstadt, K. E., Farin, M., Iverson, R. M., Obryk, M. K., Kean, J. W., Tsai, V. C., ... Logan, M. (2020). Measuring basal force fluctuations of debris flows using seismic recordings and empirical green’s functions. *Journal of Geophysical Research: Earth Surface*, 125.
- Allstadt, K. E., Matoza, R. S., Lockhart, A. B., Moran, S. C., Caplan-Auerbach, J., Haney, M. M., ... Malone, S. D. (2018). Seismic and acoustic signatures of surficial mass movements at volcanoes. *Journal of Volcanology and Geothermal Research*, 364, 76-106.
- Amarsid, L., Delenne, J. Y., Mutabaruka, P., Monerie, Y., Perales, F., & Radjai, F. (2017). Viscoinertial regime of immersed granular flows. *Physical Review E*, 96.
- Arran, M., Mangeney, A., Rosny, J. D., Farin, M., Toussaint, R., & Roche, O. (2021). Laboratory landquakes: Insights from experiments into the high-frequency seismic signal generated by geophysical granular flows. *Journal of Geophysical Research: Earth Surface*, 126, 1-25.
- Artoni, R., & Richard, P. (2015). Effective wall friction in wall-bounded 3d dense granular flows. *Physical Review Letters*, 115.
- Benage, M. C., Dufek, J., & Mothes, P. A. (2016). Quantifying entrainment in pyroclastic density currents from the tungurahua eruption, ecuador: Integrating field proxies with numerical simulations. *Geophysical Research Letters*, 43(13), 6932-6941. Retrieved from <https://agupubs.onlinelibrary.wiley.com/doi/abs/10.1002/2016GL069527> doi: <https://doi.org/10.1002/2016GL069527>
- Berzi, D., Jenkins, J. T., & Richard, P. (2020). Extended kinetic theory for granular flow over and within an inclined erodible bed. *Journal of fluid mechanics*, 885.
- Bird, R. B. R. B. (1960). *Transport phenomena*. New York: Wiley.
- Boyer, F., Élisabeth Guazzelli, & Pouliquen, O. (2011). Unifying suspension and granular rheology. *Physical Review Letters*, 107, 1-5.
- Breard, E. C., Dufek, J., Charbonnier, S., Gueugneau, V., Giachetti, T., & Walsh, B. (2023, 12). The fragmentation-induced fluidisation of pyroclastic density currents. *Nature communications*, 14, 2079.
- Breard, E. C., Dufek, J., Fullard, L., & Carrara, A. (2020). The basal friction coefficient of granular flows with and without excess pore pressure: Implications for pyroclastic density currents, water-rich debris flows, and rock and submarine avalanches. *Journal of Geophysical Research: Solid Earth*, 125, 1-22.



- Breard, E. C., Fullard, L., Dufek, J., Tennenbaum, M., Fernandez, A. N., & Dietiker, J.-F. (2022). Investigating the rheology of fluidized and non-fluidized gas-particle beds: implications for the dynamics of geophysical flows and substrate entrainment. *Granular Matter*, 24.
- Brodu, N., Delannay, R., Valance, A., & Richard, P. (2015). New patterns in high-speed granular flows. *Journal of Fluid Mechanics*, 769, 218-228.
- Campbell, C. S. (1989). The stress tensor for simple shear flows of a granular material. *Journal of fluid mechanics*, 203, 449-473.
- Campbell, C. S. (2006). Granular material flows - an overview. *Powder Technology*, 162, 208-229.
- Chmiel, M., Walter, F., Wenner, M., Zhang, Z., McArdell, B. W., & Hibert, C. (2021). Machine learning improves debris flow warning. *Geophysical Research Letters*, 48.
- Cohen, M. H., & Turnbull, D. (1959). Molecular transport in liquids and glasses. *The Journal of Chemical Physics*, 31, 1164-1169.
- Cole, S. E., Cronin, S. J., Sherburn, S., & Manville, V. (2009, 5). Seismic signals of snow-slurry lahars in motion: 25 september 2007, mt ruapehu, new zealand. *Geophysical Research Letters*, 36.
- Corwin, E. I., Jaeger, H. M., & Nagel, S. R. (2005). Structural signature of jamming in granular media. *Nature*, 435(7045), 1075-1078.
- Cruz, F. D., Emam, S., Prochnow, M., Roux, J. N., & Chevoir, F. (2005). Rheo-physics of dense granular materials: Discrete simulation of plane shear flows. *Physical Review E - Statistical, Nonlinear, and Soft Matter Physics*, 72.
- DeGiuli, E., & Wyart, M. (2017). Friction law and hysteresis in granular materials. *Proceedings of the National Academy of Sciences of the United States of America*, 114, 9284-9289.
- Delannay, R., Valance, A., Mangeney, A., Roche, O., & Richard, P. (2017). Granular and particle-laden flows: From laboratory experiments to field observations. *Journal of Physics D: Applied Physics*, 50.
- Farin, M., Mangeney, A., de Rosny, J., Toussaint, R., & Trinh, P. T. (2018). Link between the dynamics of granular flows and the generated seismic signal: Insights from laboratory experiments. *Journal of Geophysical Research: Earth Surface*, 123, 1407-1429.
- Farin, M., Mangeney, A., Toussaint, R., Rosny, J. D., Shapiro, N., Dewez, T., ... Berger, F. (2015). Characterization of rockfalls from seismic signal: Insights from laboratory experiments. *Journal of Geophysical Research: Solid Earth*, 120, 7102-7137.
- Forterre, Y., & Pouliquen, O. (2008). Flows of dense granular media. *Annual Review of Fluid Mechanics*, 40, 1-24.
- Fullard, L. A., Breard, E. C., Davies, C. E., Godfrey, A. J., Fukuoka, M., Wade, A., ... Lube, G. (2019). The dynamics of granular flow from a silo with two symmetric openings. *Proceedings of the Royal Society A: Mathematical, Physical and Engineering Sciences*, 475.
- Gardel, E., Sitaridou, E., Facto, K., Keene, E., Hattam, K., Easwar, N., & Menon, N. (2009). Dynamical fluctuations in dense granular flows. *Philosophical transactions of the Royal Society of London. Series A: Mathematical, physical, and engineering sciences*, 367(1909), 5109-5121.
- Garg, R., Li, T., Pannala, S., & Galvin, J. (2012). *Documentation of open-source mfix-dem software for gas-solids flows*. Retrieved from [https://mfix.netl.doe.gov/documentation/dem.doc\\_2012-1.pdf](https://mfix.netl.doe.gov/documentation/dem.doc_2012-1.pdf)
- George, D. L., & Iverson, R. M. (2014). A depth-averaged debris-flow model that includes the effects of evolving dilatancy. ii. numerical predictions and experimental tests. *Proceedings of the Royal Society. A, Mathematical, physical, and engineering sciences*, 470(2170).
- Gidaspow, D. (1994). *Multiphase flow and fluidization*. Boston, MA: Academic

- Press.
- Goldhirsch, I. (2008). Introduction to granular temperature. *Powder technology*, 182(2), 130-136.
- Iverson, R. M. (1997). The physics of debris flows. *Reviews of Geophysics*, 35, 245-296.
- Iverson, R. M., & George, D. L. (2014). A depth-averaged debris-flow model that includes the effects of evolving dilatancy. i. physical basis. *Proceedings of the Royal Society. A, Mathematical, physical, and engineering sciences*, 470(2170).
- Iverson, R. M., Logan, M., LaHusen, R. G., & Berti, M. (2010). The perfect debris flow? aggregated results from 28 large-scale experiments. *Journal of Geophysical Research*, 115(F3).
- Jalali, P., Ritvanen, J., & Sarkomaa, P. (2006). Stress fluctuations in monodisperse and bidisperse rapid granular shear flows. *Physica A theoretical and statistical physics*, 369(2).
- Johnson, P. C., & Jackson, R. (1987). Frictional-collisional constitutive relations for granular materials, with application to plane shearing. *Journal of Fluid Mechanics*, 176, 67-93.
- Jop, P., Forterre, Y., & Pouliquen, O. (2006). A constitutive law for dense granular flows. *Nature*, 441, 727-730.
- Josserand, C., Tkachenko, A., Mueth, D., & Jaeger, H. (2000). Memory effects in granular materials. *Physical review letters*, 85, 3632-3635.
- Kheiripour Langroudi, M., Sun, J., Sundaresan, S., & Tardos, G. (2010). Transmission of stresses in static and sheared granular beds: The influence of particle size, shearing rate, layer thickness and sensor size. *Powder technology*, 203(1), 23-32.
- Kim, S., & Kamrin, K. (2020, 8). Power-law scaling in granular rheology across flow geometries. *Physical Review Letters*, 125.
- Levy, C., Mangeney, A., Bonilla, F., Hibert, C., Calder, E. S., & Smith, P. J. (2015). Friction weakening in granular flows deduced from seismic records at the soufrière hills volcano, montserrat. *Journal of Geophysical Research: Solid Earth*, 120, 7536-7557.
- Longhi, E., Easwar, N., & Menon, N. (2002). Large force fluctuations in a flowing granular medium. *Physical review letters*, 89(4), 045501-045501.
- Lube, G., Breard, E. C., Jones, J., Fullard, L., Dufek, J., Cronin, S. J., & Wang, T. (2019). Generation of air lubrication within pyroclastic density currents. *Nature Geoscience*, 12, 381-386.
- Lube, G., Breard, E. C. P., Esposti-Ongaro, T., Dufek, J., & Brand, B. (2020). Multiphase flow behaviour and hazard prediction of pyroclastic density currents. *Nature Reviews Earth and Environment*, 1, 348-365.
- Lun, C. K., Savage, S. B., Jeffrey, D. J., & Chepur, N. (1984). Kinetic theories for granular flow: Inelastic particles in couette flow and slightly inelastic particles in a general flowfield. *Journal of Fluid Mechanics*, 140.
- Majmudar, T. S., & Behringer, R. P. (2005). Contact force measurements and stress-induced anisotropy in granular materials. *Nature*, 435, 1079-1082.
- Maxey, M. R., & Riley, J. J. (1983, 04). Equation of motion for a small rigid sphere in a nonuniform flow. *The Physics of Fluids*, 26(4), 883-889. Retrieved from <https://doi.org/10.1063/1.864230> doi: 10.1063/1.864230
- McCoy, S. W., Tucker, G. E., Kean, J. W., & Coe, J. A. (2013). Field measurement of basal forces generated by erosive debris flows. *Journal of Geophysical Research: Earth Surface*, 118, 589-602.
- Mehrabadi, M., Tanneti, S., Garg, R., & Subramaniam, S. (2015). Pseudo-turbulent gas-phase velocity fluctuations in homogeneous gas-solid flow: fixed particle assemblies and freely evolving suspensions. *Journal of Fluid Mechanics*, 770, 210-246.

- MiDi, G. D. R. (2004). On dense granular flows. *European Physical Journal E*, *14*, 341-365.
- Ness, C., & Sun, J. (2015). Flow regime transitions in dense non-brownian suspensions: Rheology, microstructural characterization, and constitutive modeling. *Physical Review E - Statistical, Nonlinear, and Soft Matter Physics*, *91*.
- Piantini, M., Gimbert, F., Korkolis, E., Rousseau, R., Bellot, H., & Recking, A. (2023). Solid concentration as a main proxy for basal force fluctuations generated by highly concentrated sediment flows. *Geophysical Research Letters*, *50*(1), e2022GL100345. Retrieved from <https://agupubs.onlinelibrary.wiley.com/doi/abs/10.1029/2022GL100345> (e2022GL100345 2022GL100345) doi: <https://doi.org/10.1029/2022GL100345>
- Pouliquen, O. (1999). Scaling laws in granular flows down rough inclined planes. *Physics of fluids*, *11*, 542-548.
- Roverato, M., Cronin, S., Procter, J., & Capra, L. (2015). Textural features as indicators of debris avalanche transport and emplacement, taranaki volcano. *Bulletin of the Geological Society of America*, *127*, 3-18.
- Shipley, S., & Sarna-Wojcicki, A. M. (1993). *Distribution, thickness, and mass of late pleistocene and holocene tephra from major volcanoes in the northwestern united states: A preliminary assessment of hazards from volcanic ejecta to nuclear reactors in the pacific northwest* (Tech. Rep.). U.S. Geological Survey.
- Siman-Tov, S., & Brodsky, E. E. (2021). Distinguishing between rheophysical regimes of fluid-saturated granular-flows using dilatancy and acoustic emission measurements. *Granular matter*, *23*(2).
- Stein, S., & Wysession, M. (2003). *An introduction to seismology, earthquakes, and earth structure*. Malden, MA: Blackwell.
- Syamlal, M., Rogers, W., & O'Brien, T. J. (1993). *MFIX Documentation Theory Guide* (Tech. Rep.). Morgantown, WV: U.S. Department of Energy.
- Tordesillas, A., Shi, J., & Tshai kiwsky, T. (2011). Stress-dilatancy and force chain evolution. *International journal for numerical and analytical methods in geomechanics*, *35*, 264-292.
- Trulsson, M., Andreotti, B., & Claudin, P. (2012). Transition from the viscous to inertial regime in dense suspensions. *Physical Review Letters*, *109*.
- Tsuji, Y., Tanaka, T., & Ishida, T. (1992). Lagrangian numerical simulation of plug flow of cohesionless particle in a horizontal pipe. *Powder Technology*, *71*, 239-250.
- Vinningland, J. L., Øistein Johnsen, Flekkøy, E. G., Toussaint, R., & Måløy, K. J. (2007). Granular rayleigh-taylor instability: Experiments and simulations. *Physical Review Letters*, *99*.
- Walsh, B., Coviello, V., Capra, L., Procter, J., & Márquez-Ramirez, V. (2020). Insights into the internal dynamics of natural lahars from analysis of 3-component broadband seismic signals at volcán de colima, mexico. *Frontiers in Earth Science*, *8*.
- Weinhart, T., Hartkamp, R., Thornton, A. R., & Luding, S. (2013). Coarse-grained local and objective continuum description of three-dimensional granular flows down an inclined surface. *Physics of Fluids*, *25*.
- Yohannes, B., Hsu, L., Dietrich, W. E., & Hill, K. M. (2012). Boundary stresses due to impacts from dry granular flows. *Journal of Geophysical Research: Earth Surface*, *117*.
- Zhang, Q., & Kamrin, K. (2017). Microscopic description of the granular fluidity field in nonlocal flow modeling. *Physical Review Letters*, *118*.